



Universiteit
Leiden
The Netherlands

Quantitative MRI and laser ablation-inductively coupled plasma-mass spectrometry imaging of iron in the frontal cortex of healthy controls and Alzheimer's disease patients

Bulk, M.; Abdelmoula, W.M.; Geut, H.; Wiarda, W.; Ronen, I.; Dijkstra, J.; Weerd, L. van der

Citation

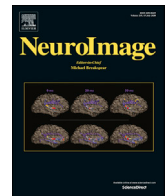
Bulk, M., Abdelmoula, W. M., Geut, H., Wiarda, W., Ronen, I., Dijkstra, J., & Weerd, L. van der. (2020). Quantitative MRI and laser ablation-inductively coupled plasma-mass spectrometry imaging of iron in the frontal cortex of healthy controls and Alzheimer's disease patients. *Neuroimage*, 215. doi:10.1016/j.neuroimage.2020.116808

Version: Publisher's Version

License: [Creative Commons CC BY 4.0 license](#)

Downloaded from: <https://hdl.handle.net/1887/3181997>

Note: To cite this publication please use the final published version (if applicable).



Quantitative MRI and laser ablation-inductively coupled plasma-mass spectrometry imaging of iron in the frontal cortex of healthy controls and Alzheimer's disease patients



Marjolein Bulk^{a,*}, Walid M. Abdelmoula^{a,b}, Hanneke Geut^{a,c}, Wim Wiarda^d, Itamar Ronen^a, Jouke Dijkstra^a, Louise van der Weerd^{a,e}

^a Department of Radiology, Leiden University Medical Center, Leiden, the Netherlands

^b Department of Neurosurgery, Brigham and Women's Hospital, Harvard Medical School, Boston, MA, USA

^c Department of Anatomy and Neuroscience, Amsterdam UMC, Vrije Universiteit Amsterdam, Amsterdam Neuroscience, Amsterdam, the Netherlands

^d Netherlands Forensic Institute, the Netherlands

^e Department of Human Genetics, Leiden University Medical Center, Leiden, the Netherlands

ARTICLE INFO

Keywords:

Alzheimer's disease
Cortex
Iron
Post mortem MRI
Mass spectrometry
QSM

ABSTRACT

Accumulation of iron within the cortex of Alzheimer's disease (AD) patients has been reported by numerous MRI studies using iron-sensitive methods. Validation of iron-sensitive MRI is important for the interpretation of *in vivo* findings. In this study, the relation between the spatial iron distribution and T₂*-weighted MRI in the human brain was investigated using a direct comparison of spatial maps of iron as detected by T₂*-weighted MRI, iron histochemistry and laser ablation-inductively coupled plasma-mass spectrometry (LA-ICP-MS), in postmortem brain tissue of the medial frontal gyrus of three control subjects and six AD patients. In addition, iron levels measured by LA-ICP-MS and three quantitative MRI methods, namely R₂* (=1/T₂*), image phase and quantitative susceptibility mapping (QSM), were compared between 19 AD and 11 controls.

Histochemistry results we obtained with the modified Meguro staining were highly correlated with iron levels as detected by LA-ICP-MS ($r^2 = 0.82$, $P < 0.0001$). Significant positive correlations were also found between LA-ICP-MS and the three quantitative MRI measurements: R₂* ($r^2 = 0.63$), image phase ($r^2 = 0.70$) and QSM ($r^2 = 0.74$ (all $p < 0.0001$)). R₂* and QSM showed the strongest correlation with iron content; the correlation of phase with iron clearly showed increased variation, probably due to its high orientation dependence. Despite the obvious differences in iron distribution patterns within the cortex between AD patients and controls, no overall significant differences were found in iron as measured by LA-ICP-MS, nor in R₂*, phase or susceptibility.

In conclusion, our results show that histochemistry as well as quantitative MRI methods such as R₂* mapping and QSM provide reliable measures of iron distribution in the cortex. These results support the use of MRI studies focusing on iron distribution in both the healthy and the diseased brain.

1. Introduction

Accumulation of iron within specific regions of the cortex of Alzheimer's disease (AD) patients has been reported by numerous studies (Acosta-Cabronero et al., 2013; van Rooden et al., 2014, 2015; Ward et al., 2014; Zecca et al., 2004; Peters et al., 2015; Lane et al., 2018). It has been suggested that this accumulation has pathological significance in AD, as well as in other neurodegenerative diseases (Ward et al., 2014; Peters et al., 2015; Hare et al., 2013). In post-mortem studies of AD brains, a high correlation between cortical iron accumulation and the

load of A β and tau pathology in the frontal cortex is reported, as well as the Braak score (Bulk et al., 2018a; van Duijn et al., 2017). Moreover, elevated cerebrospinal fluid ferritin levels have been shown to predict poorer cognition and increased risk of developing AD (Ayton et al., 2015, 2019).

Qualitative iron-sensitive MRI techniques include T₂*-weighted imaging and susceptibility-based contrasts (Haacke et al., 2005). T₂*-mapping and quantitative susceptibility mapping (QSM) can be used as quantitative proxy biomarkers for *in vivo* iron accumulation, although other sources for susceptibility changes, such as myelin, exist in the brain

* Corresponding author. Departments of Radiology and Human Genetics, Leiden University Medical Center, Albinusdreef 2, 2333 ZA, Leiden, the Netherlands.
E-mail address: m.bulk@lumc.nl (M. Bulk).

(Fukunaga et al., 2010; Langkammer et al., 2010; Wallace et al., 2016) and affect the overall tissue susceptibility (χ) as measured by MRI.

Validation of iron-sensitive MRI is important for the interpretation of in vivo findings. A number of studies have showed high correspondence between MRI and global (sub)cortical iron concentrations obtained from quantitative techniques as mass-spectrometry and proton-induced X-ray emission (PIXE) (Langkammer et al., 2010, 2012; Stuber et al., 2014). However, some of these studies reported only correlations with MRI on a global tissue level, without any spatial information and/or differential cellular iron localization. In contrast, the study by Stuber et al. showed in a detailed manner the spatial correlation between iron as measured by MRI and PIXE in primary cortical regions. In addition, the high spatial colocalization between MRI and histological iron stainings within several brain regions was demonstrated by us and others (Fukunaga et al., 2010; Stuber et al., 2014; Bulk et al., 2018b; Sun et al., 2015; Hametner et al., 2018). However, histological iron stainings are qualitative and susceptible to variation due to differences in tissue preparation and protocols (van Duijn et al., 2013). Moreover, the majority of these studies have been mostly limited to deep gray matter structures, such as the basal ganglia, which are known to contain the highest iron content in the brain. Thus to further validate MRI-based detection of cortical iron in vivo, a direct comparison between MRI, histologically detected iron and a quantitative gold standard for iron detection within the same tissue is needed.

In this study we first validated MRI-based detection of cortical iron

and iron histology using laser ablation inductively-coupled mass spectrometry (LA-ICP-MS), a well-established method for iron detection with high specificity, spatial resolution and sensitivity, to detect iron levels well below the typical biological concentrations (O'Reilly et al., 2014). We applied MRI, LA-ICP-MS and iron histology to the same tissue to obtain spatial maps of iron from each method, enabling a direct comparison among the three techniques (Fig. 1). Secondly, we measured iron levels in AD patients and controls with LA-ICP-MS and all three quantitative MRI methods to examine previously reported results of increased iron in AD.

2. Methods

2.1. Human brain samples

Formalin-fixed tissue samples of the medial frontal gyrus of 11 control subjects with no clinical or pathological signs of AD, and 19 AD patients with a clinical and confirmed pathological diagnosis of AD were included. Control subjects and AD patients were sex- and age-matched. Patient-group characteristics are presented in Table 1.

All brain tissue was obtained from the Netherlands Brain Bank (NBB, Netherlands Institute for Neuroscience Amsterdam, The Netherlands) and the Normal Aging Brain Collection (Amsterdam Neuroscience, Amsterdam UMC, Vrije Universiteit Amsterdam, The Netherlands). Following the Dutch national ethical guidelines, anonymity of all subjects

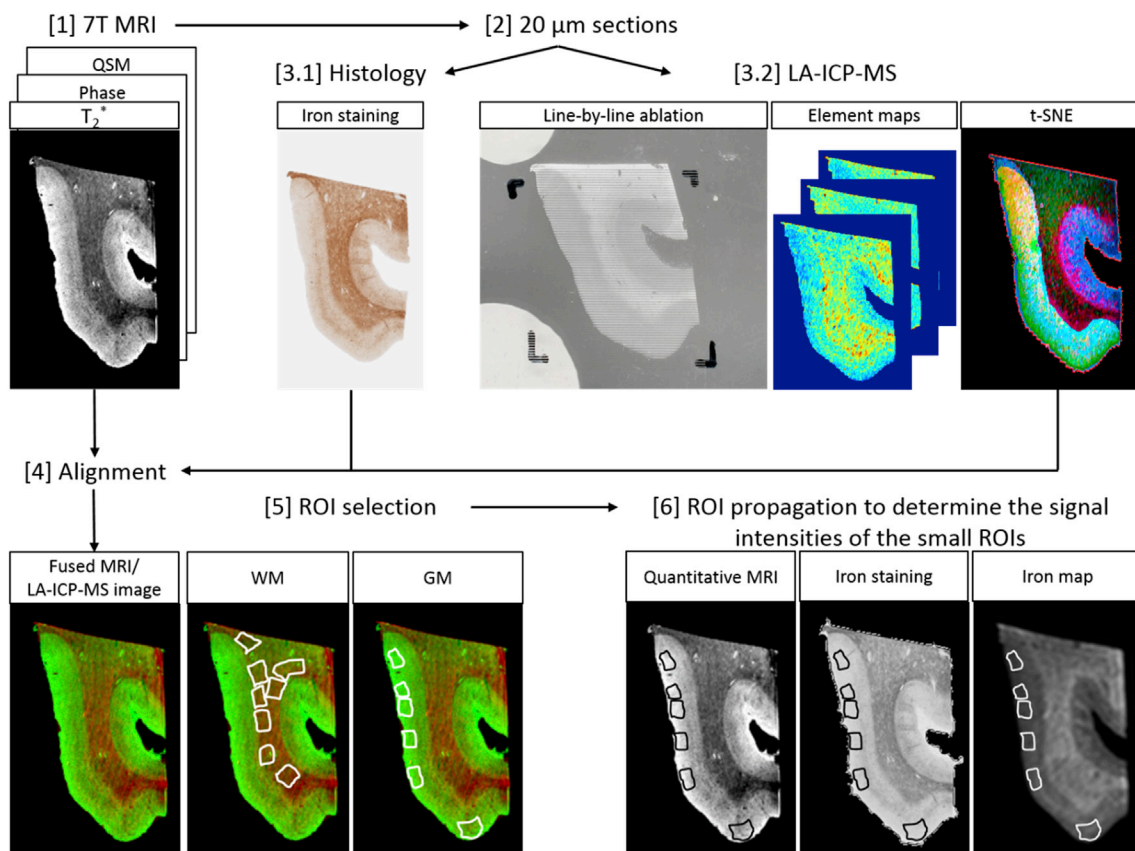


Fig. 1. Study design. [1] 7T MRI was performed on formalin fixed human tissue samples of the medial frontal gyrus. R_2^* ($=1/T_2^*$), phase, and QSM maps were reconstructed to obtain quantitative MRI data. After MRI, the same tissue was used for iron immunohistochemistry and LA-ICP-MS. [2] First, tissue blocks were embedded in paraffin and subsequently serially cut into 20- μm thick sections. One 20- μm -thick section was used for [3.1] histochemical iron detection and a section adjacent to the histological section was used for [3.2] LA-ICP-MS. [4] The histological iron image and the LA-ICP-MS image were registered to the MRI image using the non-linear dimensionality reduction algorithm of t-distributed stochastic neighbor embedding (t-SNE). [5] To investigate the correlation between LA-ICP-MS for iron detection, iron histology and quantitative MRI, multiple small regions of interest (ROI) containing only GM (covering the superficial cortical layers (layer I-III) and deep cortical layers (IV-VI)) or superficial WM were manually drawn on the aligned and fused T_2^* -weighted MRI/LA-ICP-MS images. [6] After registration, the regions of interest were projected on each of the aligned quantitative MRI maps, LA-ICP-MS iron maps and iron histological images to obtain the mean signal intensities within the annotated regions.

Table 1

Case characteristics.

	Controls (n = 11)	AD (n = 19)
Mean age at death, y (range)	82,3 (70–93)	75,6 (43–96)
Male/female	4/7	7/12
Braak stage, median (range)	2 (1–3)	6 (4–6) ^a
APOE- ϵ 4 carriers	1/6	12/19 ^a
Post-mortem interval, mean (sd)	6h:37m (1h:23m)	5h:10m (1h:16m) ^a
Duration formalin-fixation, median (range)	1 year (0–3)	1 year (0–3)

^a Indicates a significant difference between controls and AD patients with $p < 0.05$. Continuous variables were normally distributed and compared using an unpaired t -test. A chi-square test was used to compare categorical variables. Note: APOE- ϵ 4 = Apolipoprotein E ϵ 4 gene allele.

was preserved by using a coded system for the tissue samples.

Previous studies have shown that formalin fixation may affect absolute iron concentrations and tissue integrity, in particular after long-term storage (more than 4 years) (Schrag et al., 2010; van Duijn et al., 2011). Therefore, to avoid formalin-induced artefacts on MRI, only material fixed for a maximum period of four years was selected. In both control subjects and AD patients, most cases were fixed for not more than one year. No significant differences in duration of formalin fixation were found between the groups.

2.2. Post-mortem MRI acquisition

Tissue blocks of approximately $20 \times 15 \times 15 \text{ mm}^3$ were resected and put in a 15 ml tube (Greiner Bio-One). Before MRI, the tissue block was placed in phosphate buffered saline (PBS) for > 24 h. This was done to restore the MR relaxation times (T_1 , T_2 and T_2^*) closer to their values in non-fixed tissue (Shepherd et al., 2009). Before scanning, PBS was replaced with an MRI transparent, proton-free fluid (Fomblin LC08, Solvay). Care was taken to avoid the inclusion of trapped air bubbles to avoid susceptibility artefacts in the MR images.

MRI scans were performed at room temperature on a 7T horizontal bore Bruker MRI system equipped with a 23 mm receiver coil and Paravision 5.1 imaging software (Bruker Biospin, Ettlingen, Germany) (Fig. 1, step 1). Multiple gradient echo scans (3D) with a total imaging time of 210 min were acquired from each brain sample with repetition time = 75.0 ms, echo times = 12.5, 23.2, 33.9 and 44.6 ms, flip angle = 25° at $100 \mu\text{m}$ isotropic resolution with 20 signal averages.

2.3. Iron histochemistry

After MRI, the same tissue was used for iron immunohistochemistry and LA-ICP-MS (Fig. 1, step 2). First, tissue blocks were embedded in paraffin using a standard protocol for human brain tissue. During this standardized procedure the tissue was dehydrated through several ethanol baths, followed by xylene and then infiltrated with paraffin. Subsequently, tissue blocks were embedded into wax blocks and serially cut into $20\text{-}\mu\text{m}$ thick sections. Tissue sectioning was optimized in such a way that the microtome was perpendicular on the tissue specimen, to avoid having a tilted section that would complicate the histology-to-MRI registration.

One $20\text{-}\mu\text{m}$ -thick section per subject was used for histochemical iron detection using a protocol previously described (Bulk et al., 2018b; van Duijn et al., 2013) (Fig. 1, step 3.1). Sections were deparaffinized in xylene and decreasing concentrations of ethanol in water according standard pathology protocols. Finally, samples were rinsed in purified water. After deparaffinization, $20\text{-}\mu\text{m}$ -thick sections were incubated for 80 min in 1% potassium ferrocyanide, washed, and subsequently incubated for 100 min in methanol with 0.01 M NaN_3 and 0.3% H_2O_2 . Subsequently, sections were washed with 0.1 M phosphate buffer followed by 80 min incubation in a solution containing 0.025%

3'-diaminobenzidine-tetrahydrochloride (DAB, (DakoCytomation)) and 0.005% H_2O_2 in 0.1 M phosphate buffer. The reaction was stopped by washing with tap water.

2.4. Acquisition and reconstruction of LA-ICP-MS maps

For six AD patients and three controls a $20\text{-}\mu\text{m}$ -thick section adjacent to the histological section was used for LA-ICP-MS (Fig. 1, step 3.2). After deparaffinization, tissue sections were rinsed with nanopure water and dried in a horizontal laminar air flow cabinet Class 100 before analyses.

Quantitative imaging of the tissue sections was performed using a NewWave NWR193 laser ablation system (Electro Scientific Industries, Portland, OR) hyphenated to an iCAP Q ICP-MS system (Thermo Scientific, Bremen, Germany) operating in kinetic energy discrimination (KED) mode to minimize polyatomic interference. The NW193 laser ablation system was fitted with the TwoVol2 ablation cell with a 10×10 cm scanning area. Helium was used as the ablation gas at a flow rate of 0.8 L/min, with an argon make-up flow introduced after the ablation cell at a flow rate of 0.75 L/min.

Tissue sections were ablated line-by-line with a ablation speed of $100 \mu\text{m/s}$, a $60 \mu\text{m}$ spot size, ablation rate of 20 Hz and raster spacing of $200 \mu\text{m}$. Apart from ^{57}Fe , the measured elements were ^{13}C , ^{24}Mg , ^{27}Al , ^{29}Si , ^{31}P , ^{42}Ca , ^{55}Mn , ^{60}Ni , ^{63}Cu and ^{66}Zn . These elements were not within the scope of this manuscript, and therefore the data are not shown. All data are openly available upon request. The dwell time per element is 0,01 s. The laser energy and ablation rate were tuned to ablate the complete $20 \mu\text{m}$ tissue layer without ablating the underlying glass layer. The element ^{29}Si was measured to control that the glass was not affected. Before each measurement, a tuning and performance check was done to make sure the system started with an optimized sensitivity. For quality assurance, an isoprene based glue layer with known element concentrations was measured before and after measuring the tissue section. The glue layer was measured with line ablation and under the same ablation conditions. According these tests, the decrease of the iron signal after each tissue section (of a measurement of about 3 h) was about 8%. The overall reproducibility (relative standard deviation of the measurement period) based on the quality assurance standard was 14%.

The original LA-ICP-MS data were provided as a set of high dimensional vectors each of which represented an ablation line. Each ablation line held spectra of various elements distribution detected at discrete locations covered by that line. LA-ICP-MS images were reconstructed by combining all ablation lines, eventually yielding a data cube of size (x,y,z) where (x,y) was the spatial location and z was the number spectral channels. LA-ICP-MS iron maps were not calibrated using a matrix-matched tissue standard containing known iron concentrations. Currently, only matrix matched standards for frozen brain tissue exist assuming that the water content and protein composition is the same in frozen and formalin fixed tissue. As such, the obtained iron intensities are not absolute and the LA-ICP-MS maps should only be compared within this experiment. The reported iron values in counts per second were not normalized. We refer to the supplementary materials for an overview of the effect of ^{13}C and total ion current (TIC) normalization on the reported results.

2.5. Quantitative MRI reconstruction

R_2^* maps ($=1/T_2^*$) were calculated using an in-house written MATLAB pipeline. Phase images were unwrapped using temporal fitting and Laplacian-based phase unwrapping (Li et al., 2011; Schofield and Zhu, 2003). QSM maps were calculated using temporal fitting, Laplacian-based phase unwrapping, V-SHARP background field removal (Li et al., 2011; Schweser et al., 2011; Wu et al., 2012) (voxel-size $0.6 \times 0.6 \times 0.6$ mm, maximal kernel radius 25 mm) and Morphology Enabled Dipole Inversion (MEDI) (Liu et al., 2012a, 2012b) ($\lambda = 3000$) with additional model-error reduction through iterative tuning (MERIT) artefact reduction and spherical mean - value (SMV) filtering (kernel radius = 0.5 mm).

The QSM values reconstructed were inherently referenced to the averaged susceptibility value of the whole tissue block due to, in part, the fact that the frequency shift was referenced to the mean and the phase filtering process employed using the spherical mean value filters (Li et al., 2014).

2.6. Registration of histology and LA-ICP-MS to MRI

Registration of the LA-ICP-MS iron map and histological iron staining to the corresponding MRI images (R_2^* , phase and QSM) was done to determine the spatial correlations between the three different techniques (Fig. 1, step 4). Direct registration between a 2D-image (histology or LA-ICP-MS) and a 3D-MR volume is currently not feasible due to dimensionality mismatch and lack of information provided by a single 2D slice that would yield a highly sparse content compared to a dense volumetric MR image (Ferrante and Paragios, 2017). Therefore, the most similar MRI slice with respect to the given histology was selected based on the physical location of the section in the tissue block, measured by counting the number of sections taken starting at the tissue block surface. At this approximate location, the most similar MRI slice was chosen by visual comparison of clearly detectable landmarks (contours, vasculature, tears and so forth). Due to the manual selection of the most similar MRI slice, minor changes in tilt were not accounted for.

To facilitate the comparison with the histological iron staining, the digitized iron stainings were first preprocessed and then nonlinearly aligned to the corresponding MR image as previously described (Bulk et al., 2018b).

In brief, first the digitized histological images were preprocessed to exclude the background noise. The high-resolution histological images were processed using the pre-processing pipeline proposed by Abdelmoula et al. (2014). After preprocessing, down-sizing of the high-resolution histological images was done to the same range of the MRI image size, facilitating the registration initialization (Aylward and Bullitt, 2002). For nonlinear registration the parametric-based registration scheme was used in which B-Spline transformation was chosen to correct for local deformations, multi-resolution registration strategy was employed for fast convergence (4 levels of Gaussian smoothing) Unser et al. (1993) and the cost function of mutual information was used to assess the quality of multi-modal registration.

For the LA-ICP-MS images we have adopted the method proposed by Abdelmoula et al. (2014). In this method, high dimensional spectral data are projected onto a 3-dimensional space by using the non-linear dimensionality reduction algorithm of t-distributed stochastic neighbor embedding (t-SNE) (van der Maaten and Hinton, 2008). Basically, t-SNE measures the pairwise similarity between spectral data as such similar spectra are projected near each other while dissimilar ones are projected further apart. The projected data were spatially mapped from the t-SNE scatter space as such each t-SNE coordinate feature was used as separate color channel. The resultant image is called a t-SNE image and it was found structurally informative and enabled spatial registration to the MR image. For more information on spatially mapped t-SNE we refer to Abdelmoula et al., 2014 (Abdelmoula et al., 2014) and Abdelmoula et al., 2016 (Abdelmoula et al., 2016).

We based our non-linear registration on the parametric image registration method proposed by the Insight Toolkit (ITK) (Yoo et al., 2002). In this approach, the t-SNE image was used as a moving image and was non-linearly warped to be spatially matched with the fixed MRI image. The moving image was first linearly warped using Affine transformation to capture global deformation, and then non-linearly warped using BSpline transformation model to capture local deformations. The statistical metric of mutual information was used as a similarity metric to guide the registration to converge to an optimal solution. Elastix, a publicly available image registration toolbox, was used to implement this image registration method (Klein et al., 2010). Eventually, the computed transformation was applied on each single spectral image to map it to the MRI space.

Registration of both the histological as the LA-ICP-MS images to MRI space were evaluated by visually inspecting the reference and the aligned images on top of each other. Smooth transitions between structures in the different imaging modalities images was interpreted as a good registration result.

2.7. Correlation analyses

To investigate the correlation between LA-ICP-MS for iron detection, iron histology and quantitative MRI, multiple small regions of interest (ROI) containing only GM (covering the superficial cortical layers (layer I-III) and deep cortical layers (IV-VI)) or superficial WM were manually drawn on the aligned and fused T_2^* -weighted MRI/LA-ICP-MS images (Fig. 1, step 5). After registration, the regions of interest were projected on each of the aligned quantitative MRI maps, LA-ICP-MS iron maps and iron histological images. Visual examination confirmed the quality of ROIs propagation on top of the aligned images. Correlations of the mean signal intensities were computed within that annotated region for the LA-ICP-MS iron map and the histological image and the corresponding quantitative MR images (Fig. 1, step 6). In addition, mean GM and WM values were calculated per technique, per subject by averaging the total signal intensities of the smaller ROIs, indicated by the colored dots in Fig. 3.

2.8. Statistics

Correlation analyses of the mean ROI values were done using Pearson correlation. Continuous variables were first assessed for normal distribution. As no extreme outliers were detected, the continuous variables were compared using an unpaired *t*-test. A chi-square test was used to compare categorical variables. All statistical analyses were performed using Statistical Package of Social Sciences (SPSS, version 23; SPSS, Chicago, USA). A significance level of $p = 0.05$ was used.

3. Results

The distribution of iron within the frontal cortex of human brain tissue was mapped using LA-ICP-MS. In combination with iron histochemistry and T_2^* -weighted MRI data of the same tissue, the correlation between iron and quantitative MRI measures for iron detection was investigated.

Fig. 2 shows the visual correspondence of iron measured by LA-ICP-MS, iron histochemistry and T_2^* -weighted MRI. All three techniques revealed spatial variations in iron deposition in the GM and WM, with higher values indicating higher iron content in the WM compared to the GM. More specifically, iron could be located within specific patterns in both AD and control subjects, especially on iron histochemistry and T_2^* -weighted MRI. These patterns were related to cortical bands of highly myelinated fiber bundles parallel to the cortical surface (e.g. lines of Baillarger), subcortical U-fibers close to the gray-white matter boundary, and an inhomogeneous patchy iron distribution in the WM. In addition, as reported in a previous ex vivo 7T imaging study (Bulk et al., 2018b), AD patients have a different appearance of the cortex on T_2^* -weighted MRI compared to controls subjects characterized by a diffuse hypointense band-shaped pattern covering the middle layers of the cortex (III/IV), sometimes reaching layer II and V, obscuring the lines of Baillarger (Fig. 2, arrows). This diffuse hypointense band was observed on T_2^* -weighted MRI in 17/19 AD patients, whereas only in 2 control subjects was this band partially observed. As shown previously (van Duijn et al., 2017; Bulk et al., 2018b) by spatial correlation analyses of the cortical pixel intensities of MRI and histology, the diffuse hypointense band on MRI is highly correlated with increased iron accumulation and changes in cortical myelin.

To quantitatively assess the similarity in GM and WM iron distribution as seen in the relative LA-ICP-MS iron maps and those obtained from iron histochemistry and MRI, correlation analyses were carried out on

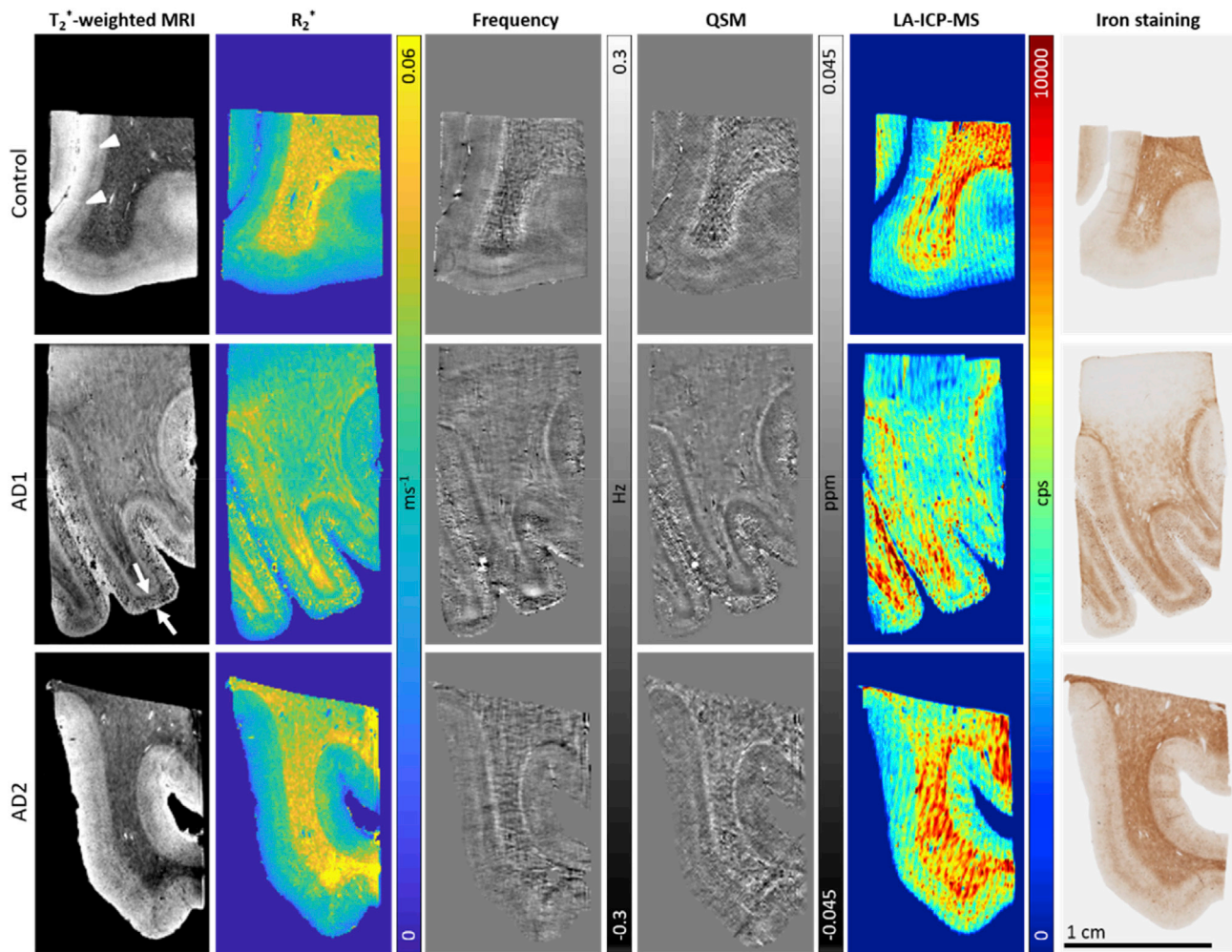


Fig. 2. Overview of quantitative MRI, relative iron map acquired with LA-ICP-MS and iron staining for one control and two AD patients. On T_2^* -weighted MRI the lowest signal amplitude was found within the myelin rich areas of the WM and lines of Baillarger (arrow head control case). As reported in a previous ex vivo 7T imaging study (Bulk et al., 2018b), the cortex of AD patients is characterized by a diffuse hypointense band-shaped pattern covering the middle layers of the cortex (III/IV), sometimes extending till layer II and V, obscuring the lines of Baillarger (arrow AD case). The same contrast patterns were found in the LA-ICP-MS iron maps and the iron staining with high iron in the myelin rich areas. Scale bar = 1 cm and applies to all modalities.

the data. Per subject, multiple small GM and WM ROIs were drawn on the T_2^* -weighted MR image and projected onto the aligned LA-ICP-MS iron map and histological iron image. The mean signal intensity within each ROI was calculated (Fig. 3, gray dots) and subsequently a mean GM and WM signal intensity was calculated per subject by averaging the mean signal intensities of the smaller ROIs (Fig. 3, colored dots). Correlations of the mean GM and WM signal intensities showed a strong positive correlation between iron as measured by LA-ICP-MS and iron histochemistry ($r^2 = 0.82$, $p < 0.0001$). Significant positive correlations were also found between LA-ICP-MS and all three quantitative MRI measurements ($r^2 = 0.63$, 0.70 and 0.74 for R_2^* , phase and χ , respectively, all $p < 0.0001$). Correlation plots using the mean signal intensities of the individual smaller GM and WM ROIs also showed significant positive correlations between LA-ICP-MS and all three quantitative MRI measurements (Fig. 3, gray dots). However, the correlations were less strong and clearly showed increased variation in phase values resulting in a lower r^2 ($r^2 = 0.50$, 0.22 and 0.42 for R_2^* , phase and χ , respectively, all $p < 0.0001$).

Iron measured by LA-ICP-MS as well as all three quantitative MRI methods were compared between AD and controls (Fig. 4). Despite the obvious differences in iron distribution patterns within the cortex between patients and controls, no overall significant differences were found in iron signal as measured by LA-ICP-MS, nor in R_2^* , phase or χ between

AD and controls.

4. Discussion

In this study, the relation between iron concentrations and T_2^* -weighted MRI in the human brain was investigated using a direct comparison of spatial distribution maps of iron as detected by T_2^* -weighted MRI, iron histochemistry and LA-ICP-MS in postmortem brain tissue.

Although histochemistry techniques to visualize iron in formalin fixed paraffin embedded human brain tissue have been shown to yield widely different results, depending on the protocols used (van Duijn et al., 2013), the modified Meguro staining used in this study was highly correlated with relative iron values as detected by LA-ICP-MS. This confirms the Meguro staining as a reliable staining procedure for iron detection in post-mortem cortices of both patients and controls. The Meguro staining is assumed to stain only for non-heme iron, mostly Fe^{3+} but also some Fe^{2+} (Meguro et al., 2007). However, due to the harsh staining conditions some heme iron might be included as well but the percentage of heme iron is assumed to be minimal as heme iron is one of the ‘masked’ iron species. Previous studies indicate that staining for heme iron requires tissue treatment with strong oxidizing agents (Pearse, 1985). The modified Meguro staining, as used in this study, only required a DAB intensification containing 0.005% H_2O_2 , we therefore assume that

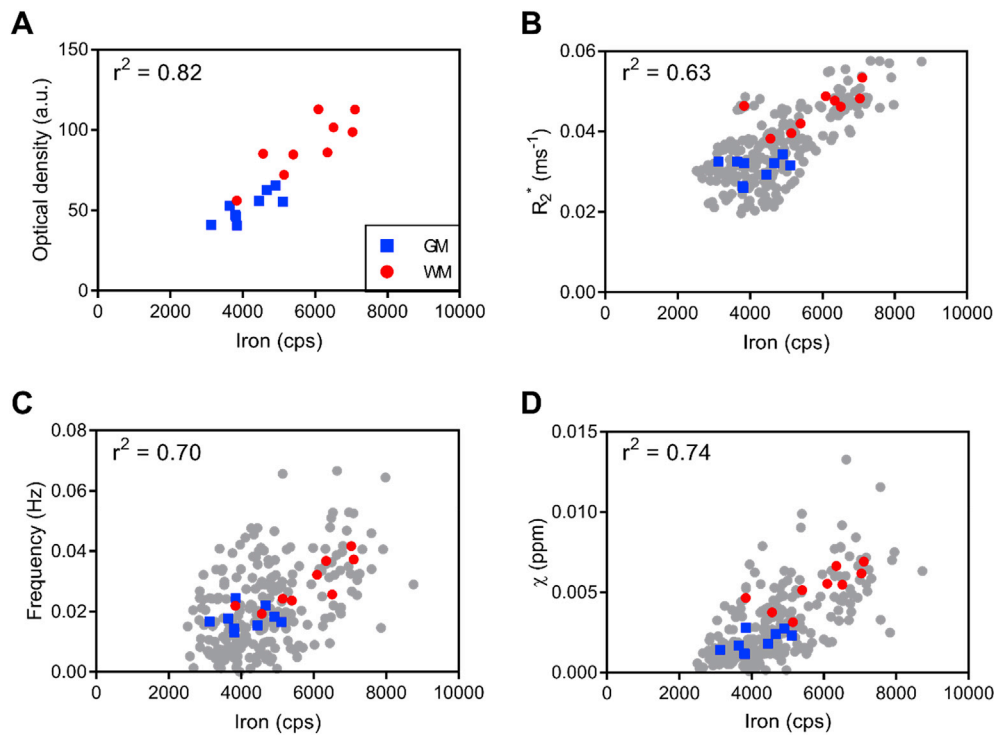


Fig. 3. Correlation plots of iron measured with LA-ICP-MS and (A) iron staining, (B) R_2^* , (C) phase, and (D) QSM. Significant positive correlations ($p < 0.0001$) were found for all imaging modalities (colored dots). Correlation plots using the mean signal intensities of the individual smaller GM and WM ROIs also showed significant positive correlations between LA-ICP-MS and all three quantitative MRI measurements (B,C,D) However, the correlations were less strong and clearly showed the increased higher variation in phase values resulting in a lower r^2 ($r^2 = 0.50, 0.22$ and 0.42 for R_2^* , phase and χ , respectively, all $p < 0.0001$). Correlation analyses of the mean ROI values were done using Pearson correlation. Blue squares: mean GM signal per subject; Red dots: mean WM signal per subject; Gray dots: mean signal intensities of the individual smaller GM and WM ROIs.

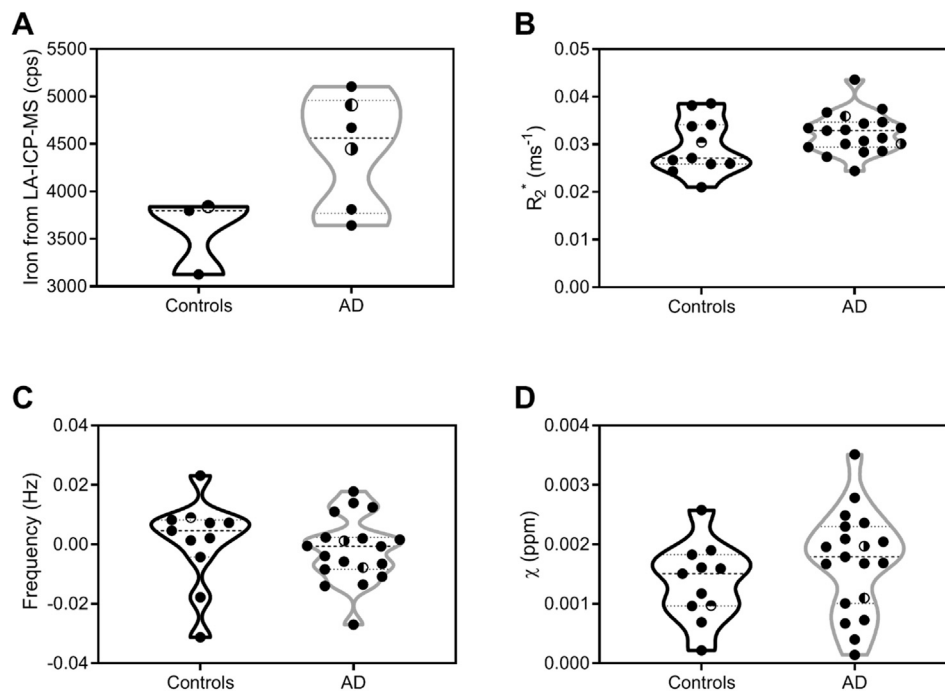


Fig. 4. Comparison of (relative) cortical iron values derived from the cortex between controls and AD patients measured with (A) LA-ICP-MS, (B) R_2^* , (C) phase, and (D) QSM. Despite the obvious spatial differences in the cortex between AD patients and controls, no overall significant differences were found in relative cortical iron values as measured by LA-ICP-MS, nor in R_2^* , phase or χ . \circ indicates the control subject, \bullet indicates AD1, and \bullet indicates AD2 from Fig. 2.

the percentage of heme iron is minimal. As LA-ICP-MS measures all iron species, the specificity of the modified Meguro staining for Fe^{3+} cannot be confirmed. LA-ICP-MS is a powerful imaging technique to produce detailed images of specific element distributions in thin tissue sections, but it is not widely available or suitable for high-throughput analyses using large case series compared to histological iron stainings which only require a standard research lab. Based on the current data,

semi-quantitative analyses of histological iron stainings should be considered as a reliable approach to assess relative brain iron increases and iron distribution within tissue samples.

The variety of existing MRI methods to detect iron accumulation in the brain reflects the fact that each MRI technique has their own disadvantages and advantages (Deistung et al., 2013). Whereas R_2^* is the measure of signal decay within a voxel influenced by susceptibility

induced field perturbations, it may also be affected by other sources such as macromolecular and water content changes making R_2^* less specific to iron (Deistung et al., 2013; Mitsumori et al., 2012). These effects are less significant in phase imaging. However, due to its non-local nature, phase imaging is highly dependent on the orientation of the object with respect to the main magnetic field (Schweser et al., 2011; Schafer et al., 2009), in particular in the presence of anisotropic structures such as white matter long-range axons. These limitations may explain the higher variation in phase values found in this study. QSM overcomes the non-locality of the magnetic field distribution and might therefore be a more reliable technique to quantify brain iron. Apart from reflecting the positive magnetic susceptibility due to the presence of iron, QSM also gives information about decreases in tissue susceptibility, caused by the presence of diamagnetic materials as myelin and calcium (Shmueli et al., 2009; Wharton and Bowtell, 2010; Liu et al., 2009). Recently, methods that separate between the positive and negative susceptibility contributions to QSM have been suggested, allowing for even better quantification of the various sources of susceptibility in tissue, including iron and amyloid beta (Gong et al., 2019). Although QSM is the most reliable of the MRI methods for iron quantification, we found that the anatomical contrast within the cortex is often better appreciated on T_2^* -weighted images. Based on our histological findings in a previous study (Bulk et al., 2018b), where we observed that both iron and myelin staining intensities are increased in the cortex of AD patients compared to controls, we hypothesize that this is probably due to a spatially coinciding increase of iron and myelin within the cortex of AD patients. Iron and myelin both increase T_2^* , whereas they generate counteracting effects on QSM maps and thus reduce the contrast (paramagnetic vs. diamagnetic shift, for iron and myelin respectively).

In this study, the correlations between LA-ICP-MS and each of the three quantitative MRI measures were highly significant, illustrating the large influence of iron on T_2^* and χ . However, as shown previously by us and others, both iron and myelin have been proven as important sources for magnetic susceptibility-based MRI contrast (Fukunaga et al., 2010; Langkammer et al., 2010; Wallace et al., 2016; Bulk et al., 2018b). The effect of myelin on T_2^* -weighted MRI has been confirmed in the cerebral cortex by the remaining susceptibility shift caused by myelin after iron extraction (Fukunaga et al., 2010). Deistung et al. (2013), and Stuber et al. (2014), reported a difference in the relation between iron and χ for GM and WM. These tissue dependent differences were explained by the contribution of myelin to χ . Although we did observe higher iron concentrations in WM than in GM, we did not calculate correlations for GM and WM separately due to the limited amount of samples ($n = 9$). Moreover, our study did not include deep gray matter or deep white matter regions which are known to have higher iron and myelin concentrations compared to other regions of the brain (Ropele and Langkammer, 2017) and would thus contribute differently to GM and WM MR contrast.

Previous studies on iron accumulation in AD reported an increase in iron concentration using several techniques. An ex vivo mass-spectrometry study reported a significant increase of iron in the frontal cortex (Hare et al., 2016). Increased phase shifts (van Rooden et al., 2014, 2015) and susceptibility values (Acosta-Cabronero et al., 2013; Moon et al., 2016; Raven et al., 2013) have been reported in AD patients compared to controls. In contrast, we did not find differences in overall iron load in the frontal cortex between AD patients and controls. This and earlier work demonstrated that rather than the iron concentration, the iron distribution within the cortex is changed in AD, defined as a diffuse mid-cortical hypointense band and visible on MRI and histology (Bulk et al., 2018a, 2018b) and confirmed by LA-ICP-MS in this study. Therefore, we hypothesize that instead of an overall increased iron load, the distribution of iron is changed in the cortex of AD patients. In addition, the variance within the AD samples is quite high which can partially be explained by the differences in age of onset of the AD patients. We and others showed previously that T_2^* -weighted contrast changes are more severe in patients who develop the disease before the age of 65 compared

to more typical AD patients who develop the disease after the age of 65²⁰.

Potential limitations of this work include using formalin fixed brain tissue. The effect of formalin fixation on MR relaxation times and iron levels are a necessary evil but unfortunately unavoidable when using human tissue. This is a limitation in any study not using fresh tissue and may hamper the comparability with results from in vivo MRI. However, correlation studies including histology and LA-ICP-MS require these kind of tissue types. Previous studies have shown that formalin fixation may affect absolute iron concentrations and tissue integrity, in particular after long-term storage (more than 4 years) (Schrage et al., 2010; van Duijn et al., 2011). Storage in formalin for shorter periods (<18 months) was shown to have no effect on iron concentrations (Gellein et al., 2008). Therefore, this study only included material fixed for a maximum period of four years and fixation duration was matched between controls and AD subjects. In addition, the preparation methods (whole brain fixation in 10% buffered formalin, excision of tissue blocks, paraffin embedding, and tissue sectioning) was identical for all samples. Another limitation is the known effect of temperature on MR relaxation times which were different than in vivo temperatures. As shown previously by Birkl et al. (2016), T_2^* within the cortex decreases by 35% as a result of formalin fixation and scanning at temperature compared to in vivo MRI. In this study all tissue blocks were scanned at room temperature, and thus the temperature effect between the samples is expected to be minimal but does not allow comparison to in vivo values. Overall, all samples were treated and scanned following a standardized protocol. As such, we assumed that all potential metal losses due to leaching, contaminations during the different treatments and the effect of temperature were the same for all cases. Lastly, a limitation is the lack of absolute values derived from the iron staining and the LA-ICP-MS iron maps. Although the reported results and correlations are thus relative, the results showed that the iron staining despite its qualitative nature as well as R_2^* and QSM are reliable techniques to visualize iron distribution in the cortex.

In conclusion, iron as detected by iron histochemistry (modified Meguro) or using R_2^* and QSM are reliable measures of iron content in the cortex. These results support the use of MRI studies focusing on iron distribution in both the healthy as diseased brain; using highly sensitive and quantitative imaging sequences iron can be non-invasively imaged and quantified in the brain. In contrast to previous studies, no differences in overall iron load in the frontal cortex between controls and AD patients were found, which may be due to the small sample size. We did observe large spatial differences in the cortical iron distribution in AD, which may indicate that iron is more likely to be redistributed than overall increased in the cortex (Bulk et al., 2018a, 2018b; van Duijn et al., 2017).

Funding

This work was supported by a grant from ZONMW program Innovative Medical Devices Initiative, project Imaging Dementia: Brain Matters (104003005) and a grant from the European Union 7th Framework Program: BrainPath (PIAPP-GA-2013–612360).

Acknowledgements

The authors thank L.M. van der Graaf for her technical assistance and J. Goeman for advise on the statistical analyses.

Appendix A. Supplementary data

Supplementary data to this article can be found online at <https://doi.org/10.1016/j.neuroimage.2020.116808>.

References

- Abdelmoula, W.M., Skraskova, K., Balluff, B., Carreira, R.J., Tolner, E.A., Lelieveldt, B.P., et al., 2014. Automatic generic registration of mass spectrometry imaging data to histology using nonlinear stochastic embedding. *Anal. Chem.* 86, 9204–9211.
- Abdelmoula, W.M., Balluff, B., Englert, S., Dijkstra, J., Reinders, M.J., Walch, A., et al., 2016. Data-driven identification of prognostic tumor subpopulations using spatially mapped t-sne of mass spectrometry imaging data. *Proc. Natl. Acad. Sci. U. S. A.* 113, 12244–12249.
- Acosta-Cabrero, J., Williams, G.B., Cardenas-Blanco, A., Arnold, R.J., Lupson, V., Nestor, P.J., 2013. In vivo quantitative susceptibility mapping (qsm) in alzheimer's disease. *PLoS One* 8, e81093.
- Aylward, S.R., Bullitt, E., 2002. Initialization, noise, singularities, and scale in height ridge traversal for tubular object centerline extraction. *IEEE Trans. Med. Imag.* 21, 61–75.
- Ayton, S., Faux, N.G., Bush, A.I., Alzheimer's Disease Neuroimaging, I., 2015. Ferritin levels in the cerebrospinal fluid predict alzheimer's disease outcomes and are regulated by apoe. *Nat. Commun.* 6, 6760.
- Ayton, S., Wang, Y., Diouf, I., Schneider, J.A., Brockman, J., Morris, M.C., et al., 2019. Brain iron is associated with accelerated cognitive decline in people with alzheimer pathology. *Mol. Psychiatr.* PMID: 30778133.
- Birkel, C., Langkammer, C., Golob-Schwarzl, N., Leoni, M., Haybaeck, J., Goessler, W., et al., 2016. Effects of formalin fixation and temperature on mr relaxation times in the human brain. *NMR Biomed.* 29, 458–465.
- Bulk, M., Kenkhuis, B., van der Graaf, L.M., Goeman, J.J., Natte, R., van der Weerd, L., 2018. Postmortem t2*-weighted mri imaging of cortical iron reflects severity of alzheimer's disease. *J Alzheimers Dis* 65, 1125–1137.
- Bulk, M., Abdelmoula, W.M., Nabuurs, R.J.A., van der Graaf, L.M., Mulders, C.W.H., Mulder, A.A., et al., 2018. Postmortem mri and histology demonstrate differential iron accumulation and cortical myelin organization in early- and late-onset alzheimer's disease. *Neurobiol. Aging* 62, 231–242.
- Deistung, A., Schafer, A., Schweser, F., Biedermann, U., Turner, R., Reichenbach, J.R., 2013. Toward in vivo histology: a comparison of quantitative susceptibility mapping (qsm) with magnitude-, phase-, and r2*-imaging at ultra-high magnetic field strength. *Neuroimage* 65, 299–314.
- van Duijn, S., Nabuurs, R.J., van Rooden, S., Maat-Schieman, M.L., van Duinen, S.G., van Buchem, M.A., et al., 2011. Mri artifacts in human brain tissue after prolonged formalin storage. *Magn. Reson. Med.* 65, 1750–1758.
- van Duijn, S., Nabuurs, R.J., van Duinen, S.G., Natte, R., 2013. Comparison of histological techniques to visualize iron in paraffin-embedded brain tissue of patients with alzheimer's disease. *J. Histochem. Cytochem.* 61, 785–792.
- van Duijn, S., Bulk, M., van Duinen, S.G., Nabuurs, R.J.A., van Buchem, M.A., van der Weerd, L., et al., 2017. Cortical iron reflects severity of alzheimer's disease. *J Alzheimers Dis* 60, 1533–1545.
- Ferrante, E., Paragios, N., 2017. Slice-to-volume medical image registration: a survey. *Med. Image Anal.* 39, 101–123.
- Fukunaga, M., Li, T.Q., van Gelderen, P., de Zwart, J.A., Shmueli, K., Yao, B., et al., 2010. Layer-specific variation of iron content in cerebral cortex as a source of mri contrast. *Proc. Natl. Acad. Sci. U. S. A.* 107, 3834–3839.
- Gellein, K., Flaten, T.P., Erikson, K.M., Aschner, M., Syversen, T., 2008. Leaching of trace elements from biological tissue by formalin fixation. *Biol. Trace Elem. Res.* 121, 221–225.
- Gong, N.J., Dibb, R., Bulk, M., van der Weerd, L., Liu, C., 2019. Imaging beta amyloid aggregation and iron accumulation in alzheimer's disease using quantitative susceptibility mapping mri. *Neuroimage* 191, 176–185.
- Haacke, E.M., Cheng, N.Y., House, M.J., Liu, Q., Neelavalli, J., Ogg, R.J., et al., 2005. Imaging iron stores in the brain using magnetic resonance imaging. *Magn. Reson. Imaging* 23, 1–25.
- Hametner, S., Endmayr, V., Deistung, A., Palmrich, P., Prihoda, M., Haimburger, E., et al., 2018. The influence of brain iron and myelin on magnetic susceptibility and effective transverse relaxation - a biochemical and histological validation study. *Neuroimage* 179, 117–133.
- Hare, D., Ayton, S., Bush, A., Lei, P., 2013. A delicate balance: iron metabolism and diseases of the brain. *Front. Aging Neurosci.* 5, 34.
- Hare, D.J., Raven, E.P., Roberts, B.R., Bogeski, M., Portbury, S.D., McLean, C.A., et al., 2016. Laser ablation-inductively coupled plasma-mass spectrometry imaging of white and gray matter iron distribution in alzheimer's disease frontal cortex. *Neuroimage* 137, 124–131.
- Klein, S., Staring, M., Murphy, K., Viergever, M.A., Pluim, J.P., 2010. Elastix: a toolbox for intensity-based medical image registration. *IEEE Trans. Med. Imag.* 29, 196–205.
- Lane, D.J.R., Ayton, S., Bush, A.I., 2018. Iron and alzheimer's disease: an update on emerging mechanisms. *J. Alzheim. Dis.* 64, S379–S395.
- Langkammer, C., Krebs, N., Goessler, W., Scheurer, E., Ebner, F., Yen, K., et al., 2010. Quantitative mr imaging of brain iron: a postmortem validation study. *Radiology* 257, 455–462.
- Langkammer, C., Schweser, F., Krebs, N., Deistung, A., Goessler, W., Scheurer, E., et al., 2012. Quantitative susceptibility mapping (qsm) as a means to measure brain iron? A post mortem validation study. *Neuroimage* 62, 1593–1599.
- Li, W., Wu, B., Liu, C., 2011. Quantitative susceptibility mapping of human brain reflects spatial variation in tissue composition. *Neuroimage* 55, 1645–1656.
- Li, W., Wu, B., Batrachenko, A., Bancroft-Wu, V., Morey, R.A., Shashi, V., et al., 2014. Differential developmental trajectories of magnetic susceptibility in human brain gray and white matter over the lifespan. *Hum. Brain Mapp.* 35, 2698–2713.
- Liu, T., Spincemaille, P., de Rochefort, L., Kressler, B., Wang, Y., 2009. Calculation of susceptibility through multiple orientation sampling (cosmos): a method for conditioning the inverse problem from measured magnetic field map to susceptibility source image in mri. *Magn. Reson. Med.* 61, 196–204.
- Liu, J., Liu, T., de Rochefort, L., Ledoux, J., Khalidov, I., Chen, W., et al., 2012. Morphology enabled dipole inversion for quantitative susceptibility mapping using structural consistency between the magnitude image and the susceptibility map. *Neuroimage* 59, 2560–2568.
- Liu, T., Xu, W., Spincemaille, P., Avestimehr, A.S., Wang, Y., 2012. Accuracy of the morphology enabled dipole inversion (medi) algorithm for quantitative susceptibility mapping in mri. *IEEE Trans. Med. Imag.* 31, 816–824.
- van der Maaten, L., Hinton, G., 2008. Visualizing data using t-sne. *J. Mach. Learn. Res.* 9, 2579–2605.
- Meguro, R., Asano, Y., Odagiri, S., Li, C., Iwatsuki, H., Shoumura, K., 2007. Nonheme-iron histochemistry for light and electron microscopy: a historical, theoretical and technical review. *Arch. Histol. Cytol.* 70, 1–19.
- Mitsumori, F., Watanabe, H., Takaya, N., Garwood, M., Auerbach, E.J., Michaeli, S., et al., 2012. Toward understanding transverse relaxation in human brain through its field dependence. *Magn. Reson. Med.* 68, 947–953.
- Moon, Y., Han, S.H., Moon, W.J., 2016. Patterns of brain iron accumulation in vascular dementia and alzheimer's dementia using quantitative susceptibility mapping imaging. *J Alzheimers Dis* 51, 737–745.
- O'Reilly, J., Douglas, D., Braybrook, J., So, P.W., Vergucht, E., Garrevoet, J., et al., 2014. A novel calibration strategy for the quantitative imaging of iron in biological tissues by la-icp-ms using matrix-matched standards and internal standardisation. *J. Anal. At. Spectrom.* 29, 1378–1384.
- Pearse, A.E.G., 1985. *Histochemistry, Theoretical and Applied*, fourth ed., 2. churchill livingstone. analytical technology.
- Peters, D.G., Connor, J.R., Meadowcroft, M.D., 2015. The relationship between iron dyshomeostasis and amyloidogenesis in alzheimer's disease: two sides of the same coin. *Neurobiol. Dis.* 81, 49–65.
- Raven, E.P., Lu, P.H., Tishler, T.A., Heydari, P., Bartzokis, G., 2013. Increased iron levels and decreased tissue integrity in hippocampus of alzheimer's disease detected in vivo with magnetic resonance imaging. *J Alzheimers Dis* 37, 127–136.
- van Rooden, S., Versluis, M.J., Liem, M.K., Milles, J., Maier, A.B., Oleksik, A.M., et al., 2014. Cortical phase changes in alzheimer's disease at 7t mri: a novel imaging marker. *Alzheimer's Dementia : J Alzheimers. Assoc.* 10, e19–26.
- van Rooden, S., Doan, N.T., Versluis, M.J., Goos, J.D., Webb, A.G., Oleksik, A.M., et al., 2015. 7t t(2)*-weighted magnetic resonance imaging reveals cortical phase differences between early- and late-onset alzheimer's disease. *Neurobiol. Aging* 36, 20–26.
- Ropele, S., Langkammer, C., 2017. Iron quantification with susceptibility. *NMR Biomed.* 30.
- Schafer, A., Wharton, S., Gowland, P., Bowtell, R., 2009. Using magnetic field simulation to study susceptibility-related phase contrast in gradient echo mri. *Neuroimage* 48, 126–137.
- Schofield, M.A., Zhu, Y., 2003. Fast phase unwrapping algorithm for interferometric applications. *Opt. Lett.* 28, 1194–1196.
- Schrag, M., Dickson, A., Jiffry, A., Kirsch, D., Vinters, H.V., Kirsch, W., 2010. The effect of formalin fixation on the levels of brain transition metals in archived samples. *Biomaterials* 31, 1123–1127.
- Schweser, F., Deistung, A., Lehr, B.W., Reichenbach, J.R., 2011. Quantitative imaging of intrinsic magnetic tissue properties using mri signal phase: an approach to in vivo brain iron metabolism? *Neuroimage* 54, 2789–2807.
- Shepherd, T.M., Thelwall, P.E., Stanisz, G.J., Blackband, S.J., 2009. Aldehyde fixative solutions alter the water relaxation and diffusion properties of nervous tissue. *Magn. Reson. Med.* 62, 26–34.
- Shmueli, K., de Zwart, J.A., van Gelderen, P., Li, T.Q., Dodd, S.J., Duyn, J.H., 2009. Magnetic susceptibility mapping of brain tissue in vivo using mri phase data. *Magn. Reson. Med.* 62, 1510–1522.
- Stuber, C., Morawski, M., Schafer, A., Labadie, C., Wahnert, M., Leuze, C., et al., 2014. Myelin and iron concentration in the human brain: a quantitative study of mri contrast. *Neuroimage* 93 (Pt 1), 95–106.
- Sun, H., Walsh, A.J., Lebel, R.M., Blevins, G., Catz, I., Lu, J.Q., et al., 2015. Validation of quantitative susceptibility mapping with perls' iron staining for subcortical gray matter. *Neuroimage* 105, 486–492.
- Unser, M.A., Aldroubi, A., Gerfen, C.R., 1993. Multiresolution image registration procedure using spline pyramids. In: *Proceedings Volume 2034, Mathematical Imaging: Wavelet Applications in Signal and Image Processing*.
- Wallace, M.N., Cronin, M.J., Bowtell, R.W., Scott, I.S., Palmer, A.R., Gowland, P.A., 2016. Histological basis of laminar mri patterns in high resolution images of fixed human auditory cortex. *Front. Neurosci.* 10, 455.
- Ward, R.J., Zucca, F.A., Duyn, J.H., Crichton, R.R., Zecca, L., 2014. The role of iron in brain ageing and neurodegenerative disorders. *Lancet Neurol.* 13, 1045–1060.
- Wharton, S., Bowtell, R., 2010. Whole-brain susceptibility mapping at high field: a comparison of multiple- and single-orientation methods. *Neuroimage* 53, 515–525.
- Wu, B., Li, W., Guidon, A., Liu, C., 2012. Whole brain susceptibility mapping using compressed sensing. *Magn. Reson. Med.* 67, 137–147.
- Yoo, T.S., Ackerman, M.J., Lorensen, W.E., Schroeder, W., Chalana, V., Aylward, S., et al., 2002. Engineering and algorithm design for an image processing api: a technical report on itk—the insight toolkit. *Stud. Health Technol. Inf.* 85, 586–592.
- Zecca, L., Youdim, M.B., Riederer, P., Connor, J.R., Crichton, R.R., 2004. Iron, brain ageing and neurodegenerative disorders. *Nat. Rev. Neurosci.* 5, 863–873.